Journal of Structural Geology 177 (2023) 104983

Contents lists available at ScienceDirect

Journal of Structural Geology

journal homepage: www.elsevier.com/locate/jsg

Lithospheric contraction concentric to Tharsis: 3D structural modeling of large thrust faults between Thaumasia highlands and Aonia Terra, Mars

A. Herrero-Gil [a], I. Egea-González [b], A. Jiménez-Díaz [c], S. Rivas Dorado [a], L.M. Parro [a,d,e], C. Fernández [a], J. Ruiz [a], I. Romeo [a,*]

[a] Departamento de Geodinámica, Estratigrafía y Paleontología, Universidad Complutense de Madrid, 28040, Madrid, Spain
[b] Departamento de Física Aplicada, Escuela Superior de Ingeniería, Universidad de Cádiz, 11519, Puerto Real, Cádiz, Spain
[c] Departamento de Biología y Geología, Física y Química Inorgánica, ESCET, Universidad Rey Juan Carlos, Móstoles, Madrid, 28933, Spain
[d] Lunar and Planetary Laboratory, University of Arizona, USA
[e] Instituto Universitario de Física Aplicada a las Ciencias y las Tecnologías, Universidad de Alicante, 03690, San Vicente del Raspeig, Alicante, Spain

ARTICLE INFO

Keywords:
3D structural modeling
Mars
Lobate scarp
Thrust fault
Tharsis

ABSTRACT

Large thrust faults on Mars are caused by lithospheric planetary contraction. The geometry of these faults is linked with the mechanical behavior of the lithosphere. Tharsis, the largest volcano-tectonic province on Mars, controls the global tectonic pattern of the planet. Here, we present a study of five large thrust faults concentric to Tharsis, located between the Thaumasia Highlands and the Argyre impact basin. We applied a 3D structural modeling, using a combination of fault-parallel flow and trishear algorithms to estimate the geometry and kinematics of the faults at depth. The modeled faults show an upper planar part dipping 33° to 40°, rooting with a listric geometry into horizontal levels at 13–27 km depth, with fault slips of 801–3366 m. The general out-of-Tharsis vergence, the listric fault geometries and the deepening of the depth of faulting toward Thaumasia outline an incipient thrust wedge architecture. Assuming that the largest faults rooted at the Brittle-Ductile Transition, we calculate a heat flow at the time of faulting of 24–54 mW m^{-2}. The obtained strength envelopes for dry and wet conditions show that all the strength of the lithosphere was located in the upper half of the crust.

Herrero-Gil, A.: Structural modeling, figure preparation **Egea-González, I.:** Heat flow calculations, figure preparation **Jiménez-Díaz, A.:** Strength envelope calculations, figure preparation **Rivas Dorado, S.:** text reviewing **Parro, L. M.:** text editing **Fernández, C.:** text reviewing, figure preparation **Ruiz, J.:** heat flow and rheology section supervision, writing **Romeo, I.:** Structural geology supervision, figure editing, writing.

1. Introduction

Large ridges with an arcuate surface trace and an asymmetric cross-view, so called lobate scarps, are among the most prominent tectonic structures found on the surface of terrestrial planets. They have been interpreted as caused by the brittle failure of the lithosphere undergoing horizontal shortening which generates large thrust faults and associated surface folding (e.g. Chicarro et al., 1985; Watters, 1993; Watters and Robinson, 1999; Watters et al., 2000; Klimczak et al., 2018; Atkins et al., 2022). The lithospheric compressional stresses responsible of large thrust faults formation are caused by the inner planetary cooling and subsequent shrinking (Nahm and Schultz, 2011) providing a global distribution of contractional structures (Knapmeyer et al., 2006, 2008; Andrews-Hanna and Broquet, 2023). Since the orientation of the maximum compressional horizontal stress is undetermined during planetary contraction at a global scale, the superposition of regional stress fields due to variations of the crustal and lithospheric thickness (Mege and Masson, 1996), and lithospheric flexure driven by regional loads (McGovern and Solomon, 1993), control the orientation of the maximum horizontal compression and consequently the strike of large thrust faults.

Contractional tectonic structures on Mars, including lobate scarps and wrinkle ridges, are concentrically developed on the Martian highlands South and Southwest of the Tharsis-Thaumasia rise (e.g. Dohm et al., 2001; Knapmeyer et al., 2006, 2008). Previous works analyze the general properties of the thrust faults in the Thaumasia highlands (Grott

* Corresponding author.
E-mail address: iromeobr@ucm.es (I. Romeo).

https://doi.org/10.1016/j.jsg.2023.104983
Received 28 March 2023; Received in revised form 25 September 2023; Accepted 18 October 2023
Available online 20 October 2023

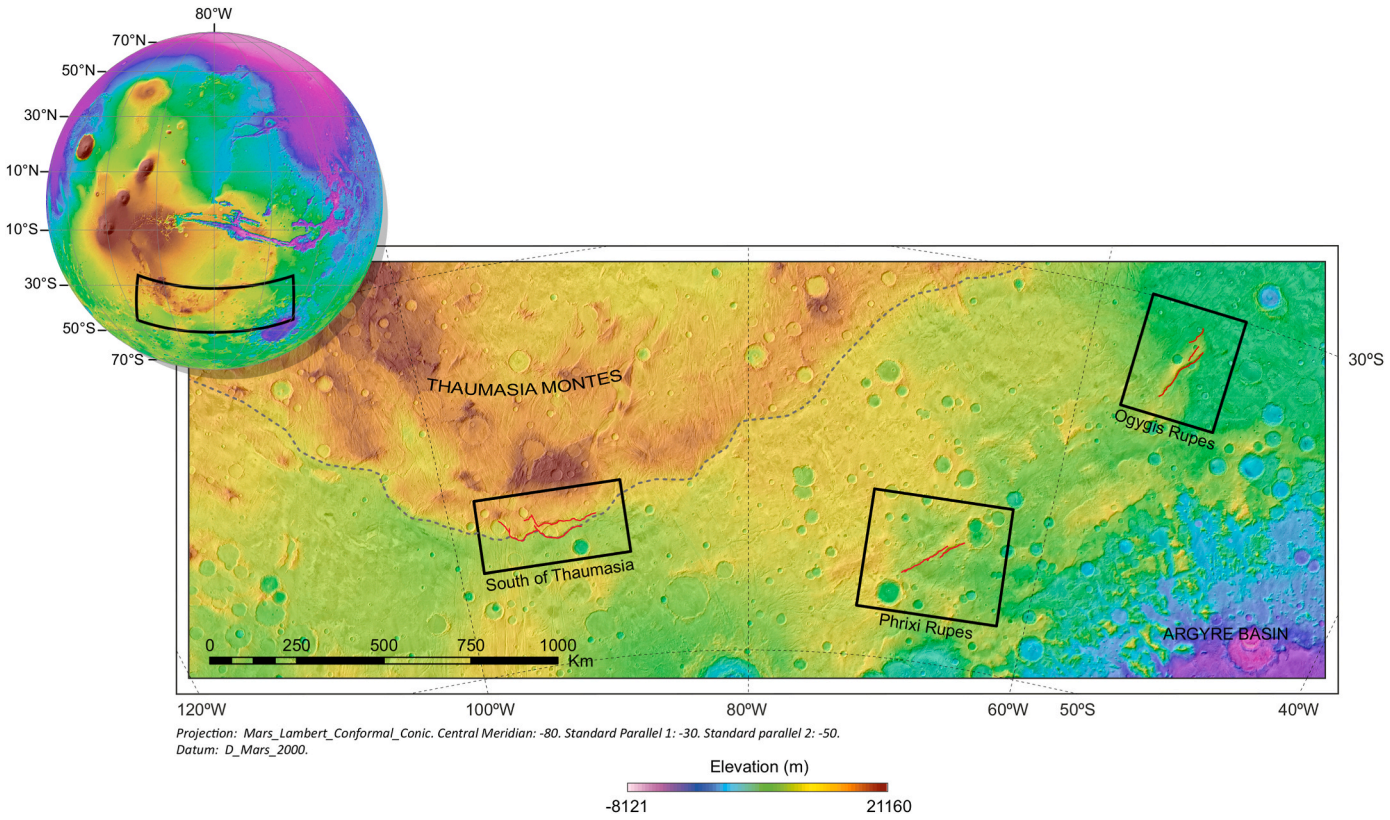

Fig. 1. Location of the modeled thrust faults (red lines) between Thaumasia Montes and Argyre impact basin. The base map is made by combining a MOLA model (DEM) over a THEMIS-IR Day image. The inset globe shows the location of the study area. (For interpretation of the references to color in this figure legend, the reader is referred to the Web version of this article.)

et al., 2007) and in the region between the Thaumasia and Argyre boundaries (Herrero-Gil et al., 2019) through 2D methods. Here we focused on the detailed structural modeling of the most prominent lobate scarps distributed along this region (Fig. 1). The recent development of advanced 3D structural modeling techniques allows us to infer the kinematics and geometry of the underlying large faults together with the structure of each individual feature, usually affected by subsidiary faults. A combination of a fault-parallel flow algorithm (Ziesch et al., 2014) to model the movement of the hanging wall over the footwall, together with a fault-propagation fold modeled by a trishear algorithm (Allmendinger, 1998; Erslev, 1991) above a propagating fault tip, has been previously applied to Ogygis Rupes (Herrero-Gil et al., 2020a), a simple lobate scarp located in the study area, and also in the complex fault system of the Amenthes region (Herrero-Gil et al., 2020b) with satisfactory results when reproducing the topography of these structures.

The large thrust fault belt concentric to Tharsis is among the most prominent contractional systems developed on the Martian lithosphere during planetary shrinking. This contractional system is specially well developed towards the South and Southeast of Tharsis where the basement of the Thaumasia block overthrusts the younger materials located to the south. In the present study, we have selected two different areas (Fig. 1) to provide detailed 3D structural models: (1) the lobate scarps identified at the south of Thaumasia Montes (located between the uplifted Noachian basement of Thaumasia in the Warrego Rise region and Aonia Terra to the south); and (2) Phrixi Rupes (located in Aonia Terra). We discuss our new results, together with the structural model of Ogygis Rupes (Herrero-Gil et al., 2020a), in the context of lithospheric planetary contraction concentric to Tharsis during the Late Noachian-Early Hesperian, the time when these structures formed. Finally, assuming that the largest depths of faulting can be considered a proxy for the Brittle-Ductile Transition (BDT), we calculate the heat flow at the time of formation together with the lithospheric strength envelope taking into account the Martian crustal models constrained by InSight.

2. Data and methods

2.1. Data for structural mapping and modeling

The structural mapping of each individual tectonic feature, including surface rupture traces of the main faults and the subsidiary structures, the anticlines and synclines generated by the fault-propagation folding, the traces of small wrinkle ridges and, in some locations, normal faults forming grabens, have been performed on images of the daytime infrared (IR) model of the Thermal Emission Imaging System (THEMIS, Mars Odyssey mission) with a 100 m/pixel resolution (Christensen et al., 2004; Edwards et al., 2011) (data available at ASU, 2010). Context Camera images (CTX, Mars Reconnaissance Orbiter, Malin et al., 2007) were used when a detailed view of the morphological characteristics of a specific structure was needed. The topographic data used during structural mapping and for the 3D structural modeling were obtained from the Mars Orbiter Laser Altimeter data (MOLA, Mars Global Surveyor) with ~463 m/pixel of horizontal resolution and ±3 m of vertical resolution (Smith et al., 2001) (data available at NASA PDS, 2014).

2.2. Structural modeling procedure

The 3D modeling was performed using the MOVE™ software suite (Petroleum Experts Ltd.). This software simulates 3D deformation including fault movement and associated folding. A successful geometrical algorithm combination for the reproduction of thrust faulting and folding under compression is the use of fault-parallel flow for the hanging wall reproducing fault accommodation folds (Egan et al., 1997; Ziesch et al., 2014) and trishear for the generation of fault-propagation

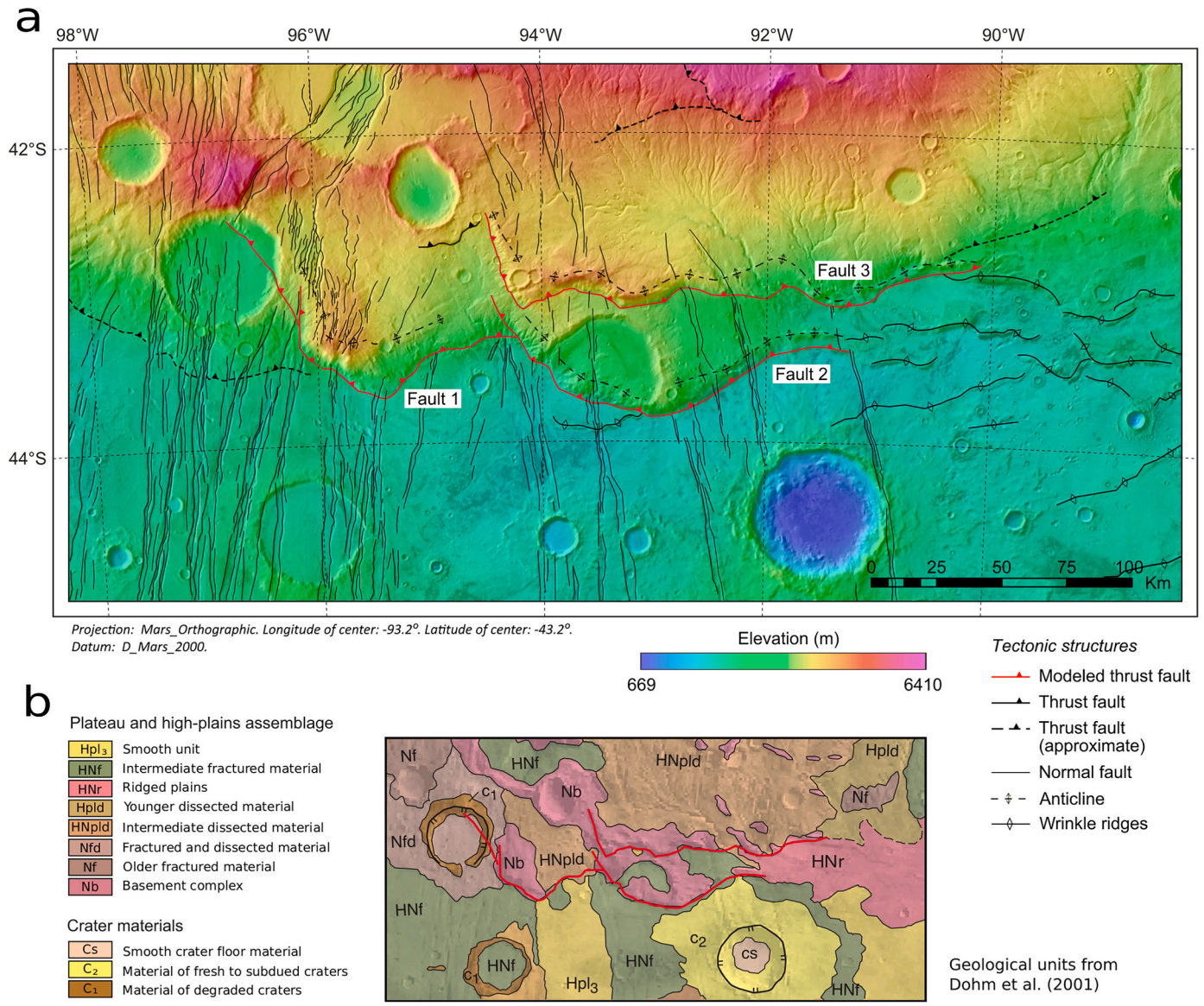

Fig. 2. a) Detailed structural map of the southern margin of Thaumasia Montes. The base map combines a MOLA model (DEM) over a THEMIS-IR Day image. The modeled large thrust faults are labeled and marked in red. The fault-propagation anticlines generated on the hanging wall of every modeled thrust are mapped. Other minor thrust faults and wrinkle ridges colored in black were not included in the models. N–S striking normal faults are also mapped. b) Geological units of the same area from Dohm et al. (2001), the traces of the studied faults are marked in red. (For interpretation of the references to color in this figure legend, the reader is referred to the Web version of this article.)

folding ahead of the propagating fault tip (Erslev, 1991; Allmendinger, 1998).

A first order approximation of the 3D fault geometry and slip distribution was obtained through the retrodeformation of the fault movement, which implies the unfolding of the topographic surface. We assume that erosion and sedimentation had a minor impact on the tectonically-driven topography (Golombek and Bridges, 2000) based on the minor activity of the water cycle since the Early Hesperian (e.g., Carr and Head, 2010).

This first approximation to the fault geometries and slip magnitude and distribution were later used as a starting point for reproducing the observed topography through a forward modeling procedure. The forward modeling needs an initial topographic surface free of tectonic deformation. This surface was generated by removing the topographic expression of each tectonic structure and impact crater when present. The removal of topography associated with impact craters is mandatory because it is not possible to separate the topographic signature of craters from that of tectonism when both structures spatially overlap. The initial topographic surface for the forward modeling was carefully generated by removing the nodes from the digital elevation model corresponding to crater depressions, rims, ejecta and structural reliefs from lobate scarps. A new digital elevation model is produced by interpolating from the remanent data using the kriging geostatistical procedure.

The modeling through forward fault slip with rupture propagation, together with the associated folding of the hanging wall and ahead of the fault tip, try to reproduce the observed topography (excluding impact craters). The forward modeling provides a fine adjustment of the parameters simulating fault tip propagation together with the trishear configuration and the slip distribution along the fault trace. Initially, we use, for the forward modeling procedure, the fault geometries and the slip distribution obtained during the restoration modeling. The final adjustment of the fault slip distribution, the trishear angle and the propagation to slip ratio were obtained by iteratively comparing the resulting modeled surface to the original MOLA topography until the best possible fit is achieved. A detailed explanation of the modeling procedure was described in Herrero-Gil et al. (2020a,b).

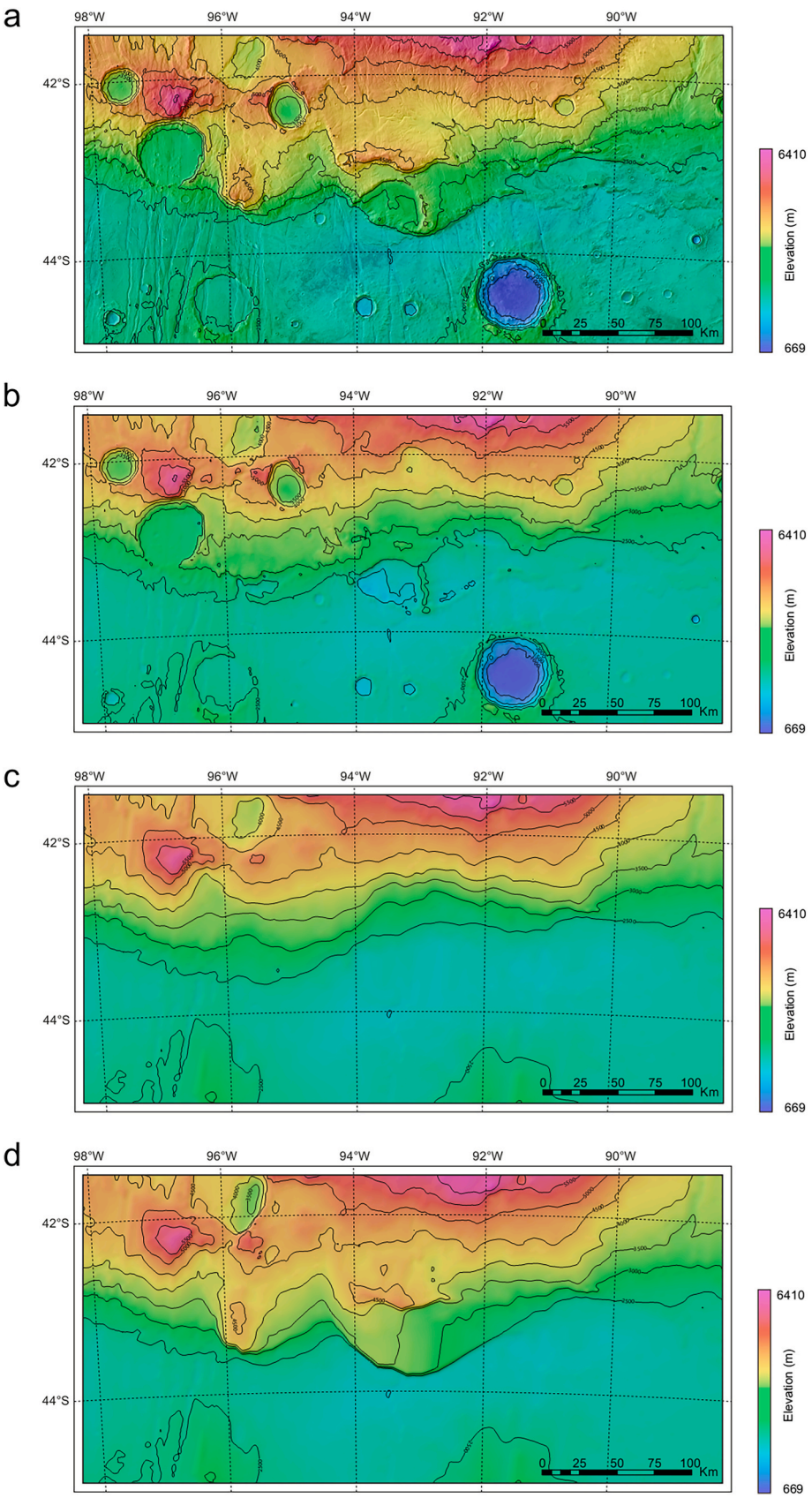

Fig. 3. Digital elevation models used and obtained during the modeling of South Thaumasia faults. a) Observed MOLA topography. b) Restored digital elevation model after the retrodeformation of the three modeled faults. c) Smooth digital elevation model where the relief caused by faults and impact craters have been removed (this topography was used as the starting stage for the 3D forward modeling). d) Digital elevation model obtained at the end of the forward modeling reproducing the main relief signatures associated with the faults observed in (a).

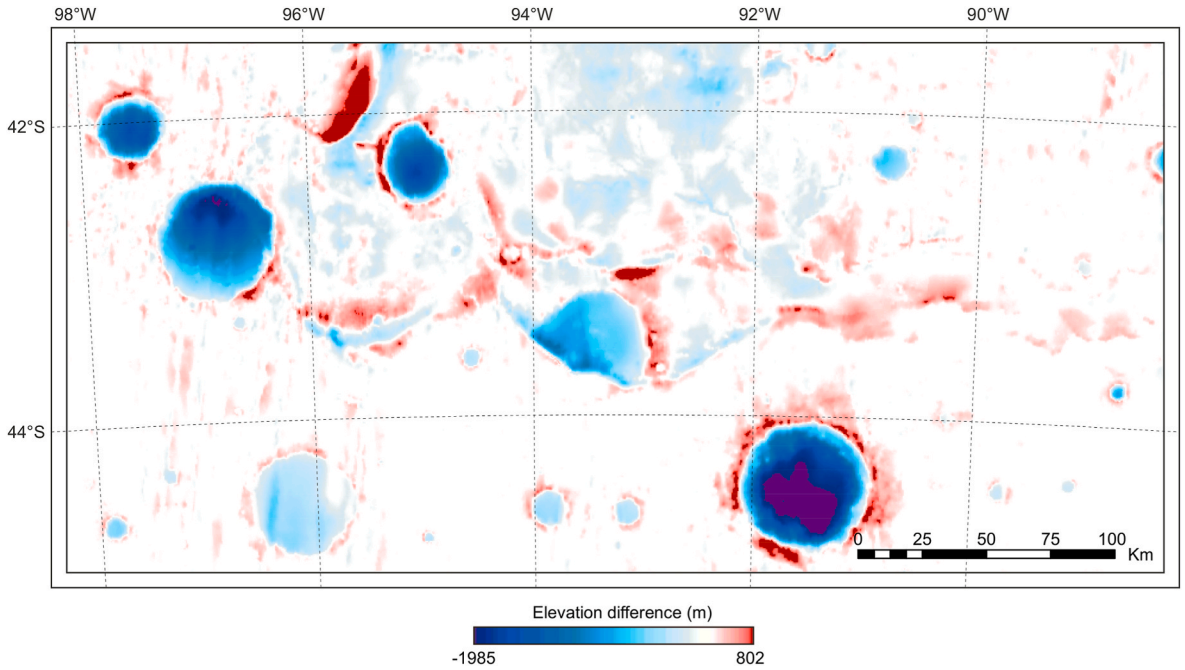

Fig. 4. Misfit of the 3D forward modeled topography with the observed MOLA topography for the South Thaumasia faults. Zero values are shown in white color indicating a good fit, note that the main error sources came from impact cratering that was not reproduced during forward modeling. (For interpretation of the references to color in this figure legend, the reader is referred to the Web version of this article.)

3. Modeling results

3.1. South-Thaumasia thrust faults

The large thrust faults bounding Thaumasia Montes toward the south are among the most prominent structures in the study area (Fig. 2a). Three main faults (marked in red color in Fig. 2a), with well-developed fault-propagation anticlines in the hanging wall, were selected for 3D structural modeling. All the modeled structures verge toward the south. Fault 1 and adjacent Fault 2 can be considered two segments of a main thrust fault. Both faults show an arcuate trace, which western terminations probably represent oblique lateral thrust ramps with a right lateral strike-slip component. Faults 1 and 2 limit two different terrains: the hanging wall (north) is represented by the uplifted Thaumasia units, while the footwall (south) is formed by smoother plains with a lower crater density (see the geological map of the area from Dohm et al. (2001) in Fig. 2b). The southern units are probably a volcano-sedimentary cover on an old heavy cratered basement, since large partially covered craters are present to the south. Probably the southern smooth plains (including HNf, HNr and Hpl_3 from Dohm et al., 2001, Fig. 2b) postdate, at least in part, the fault movement, reducing the observable structure height. Therefore, the modeled slips of Faults 1 and 2 are minimum estimates. The eastern termination of Fault 2 shows that the last contraction stages of this fault were registered by the southern plains (which were emplaced when the faults were already present, HNr from Dohm et al., 2001, Fig. 2) accommodating and distributing the contractional deformation through a set of wrinkle ridges. Fault 3, characterized by a more sinuous trace, strikes parallel to Fault 2 toward the north, and in this case both fault blocks are made of the same Thaumasia rough cratered units. Although, the surface used as a marker for deformation (fault slip) in Fault 3 is the same from both blocks the modeled fault slip represents a minimum estimation considering the abundant fluvial landforms at the northern block which probably reduced the structural relief trough erosion. A set of N–S striking grabens cross-cuts all the geological units and contractional tectonic features (lobate scarps and wrinkle ridges) being the last tectonic structures formed in the area.

The retrodeformation of the three large faults applied to the observed topography (Fig. 3a) provides a surface where the fault scarps and the associated anticlines have mostly disappeared (Fig. 3b), resulting in a surface with a homogeneous slope. Note that the large regional topographic relief associated with Thaumasia Montes cannot be explained only by the movement of these faults, remaining present at the north of Fig. 3b. A refining of the fault geometries and kinematics was obtained through the forward deformation of an ideal initial topographic surface where the local topographic variations associated with the lobate scarps and impact craters were removed (Fig. 3c). The obtained final modeled topography is shown in Fig. 3d, where a good reproduction of the observed topography (excluding impact craters) was obtained. The misfit map between the modeled and observed topography is shown in Fig. 4. The highest errors observed are caused by impact craters (impact topography was not reproduced during modeling). Consequently, the numerical calculation of the difference between the observed topography (Fig. 3a) and the forward-modeled topography (Fig. 3d) has been made excluding crater values. The median value of the error is ~ -1 m. The quartile deviation associated with this median value, which is indicative of the average fit of the model, is ~37 m, indicating that half of the values obtained when comparing these two surfaces are concentrated between 36 and −38 m.

The resultant modeled geometry of the faults is shown in Fig. 5. Similarly to other large faults underlying lobate scarps modeled on Mars (Herrero-Gil et al., 2020a, 2020b), they show a planar geometry of the upper zone followed by a listric geometry rooting into a horizontal decollement. The obtained fault parameters are compiled in Table 1. The values of fault dip correspond to the upper planar part. Ranges of values of fault dip and detachment depth indicated lateral variations of the 3D model. The southern thrust front of Thaumasia (Faults 1 and 2) shows significant minimum fault slips (3366 and 2431 m respectively) and they root into a deep detachment level at 17–27 km. Fault 3 shows a total slip of 2643 m transmitted from a shallower decollement (13–15 km). The slip distribution along strike is detailed for each fault in Fig. 6 together with the cumulative horizontal shortening transmitted from the decollement levels, which reaches a maximum of 5000 m where the displacements of Faults 2 and 3 overlap. The shape of the

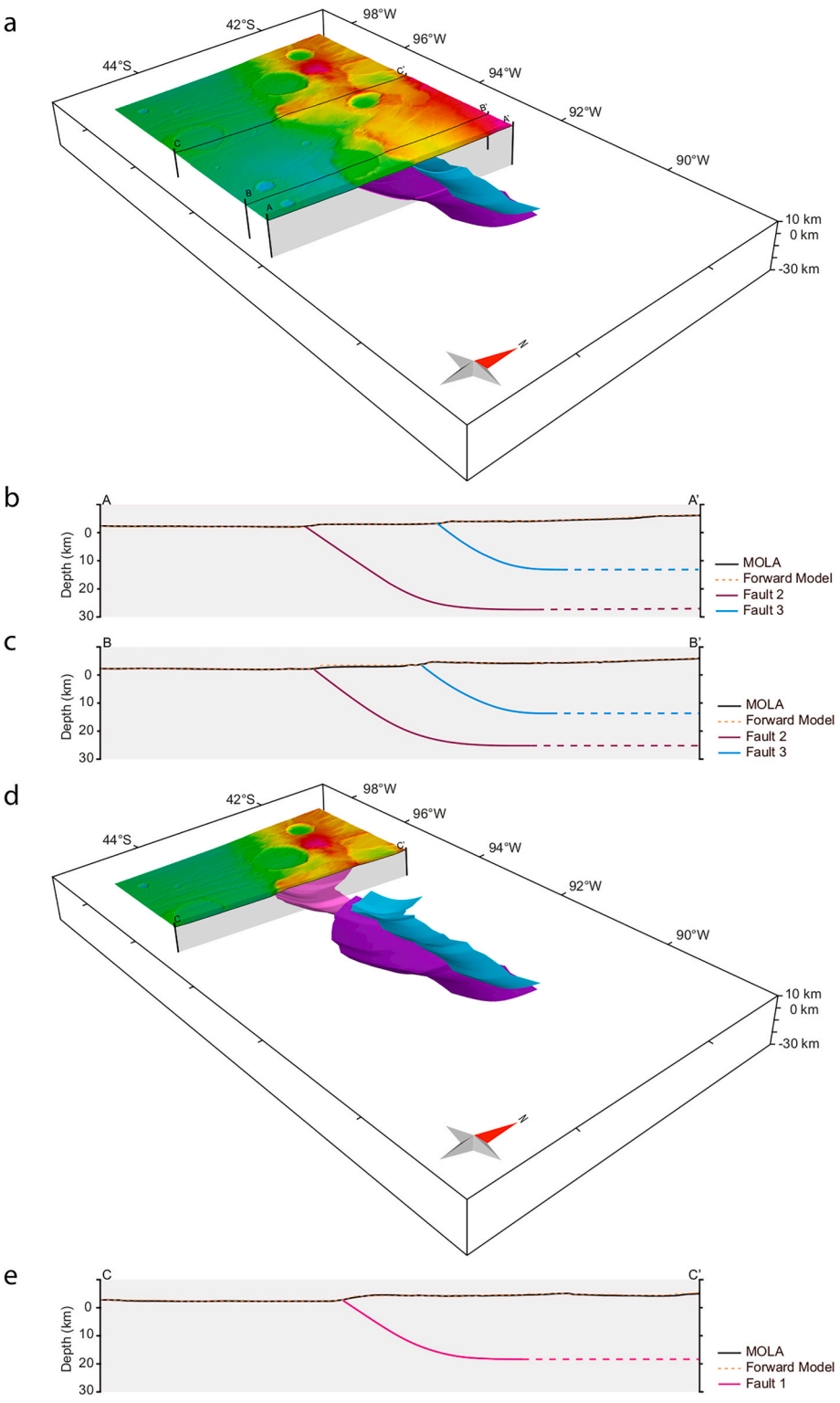

Fig. 5. South Thaumasia modeled fault geometries. (a) Perspective of the 3D model of the South Thaumasia Faults where MOLA topographic surface has been hidden east of A-A′ to show the underlying planes of Fault 2 and 3. (b) Cross Section A-A′ perpendicular to the mean strike of the faults showing a listric geometry at depth for Faults 2 and 3. (c) Cross Section B–B′ showing the geometry of Faults 2 and 3. (d) Perspective of the 3D model of the South Thaumasia Faults where MOLA topographic surface has been hidden east of C–C′ to show the underlying plane of Fault 1. (e) Cross Section C–C′ perpendicular to the mean strike of the faults showing a listric geometry at depth for Fault 1.

fault-propagating folds have been reproduced using trishear angles between 60 and 70°, with propagation to slip ratios 2.5–3 and initial tip points at −4000 to −2000 m of elevation.

3.2. *Phrixi Rupes*

This fault system is located between Thaumasia Montes and Argyre impact basin (Fig. 1) striking NE-SW. It is composed of two parallel

Table 1
Compilation of fault parameters obtained for different faults modeled around Thaumasia Montes.

	Length	Maximum slip (m)	Dip (°)	Depth (km)	Trishear angle	P/S ratio	Fault tip elevation (m)
South Thaumasia Fault 1 (This study)	113	3366	33–34	17–21	70	3	−4000
South Thaumasia Fault 2 (This study)	159	2431	34–38	21–27	70	3	−2000
South Thaumasia Fault 3 (This study)	157	2643	37–40	13–15	60	2.5	−2200
Phrixi Fault 4 (This study)	157	801	33.6	16–17	85	3	0
Phrixi Fault 5 (This study)	90	2847	33	16–19	89	3	−4000
Ogygis Rupes Main fault (Herrero-Gil et al., 2020a)	220	2850	39	17.2–17.8	76 (center), 70 (edges)	3	−4700
Ogygis Rupes Backthrust 1 (Herrero-Gil et al., 2020a)	60	1200	22	2.3–2.9	70	2	−750
Ogygis Rupes Backthrust 2 (Herrero-Gil et al., 2020a)	65	1800	23	5.5–5.6	36	2	−1200

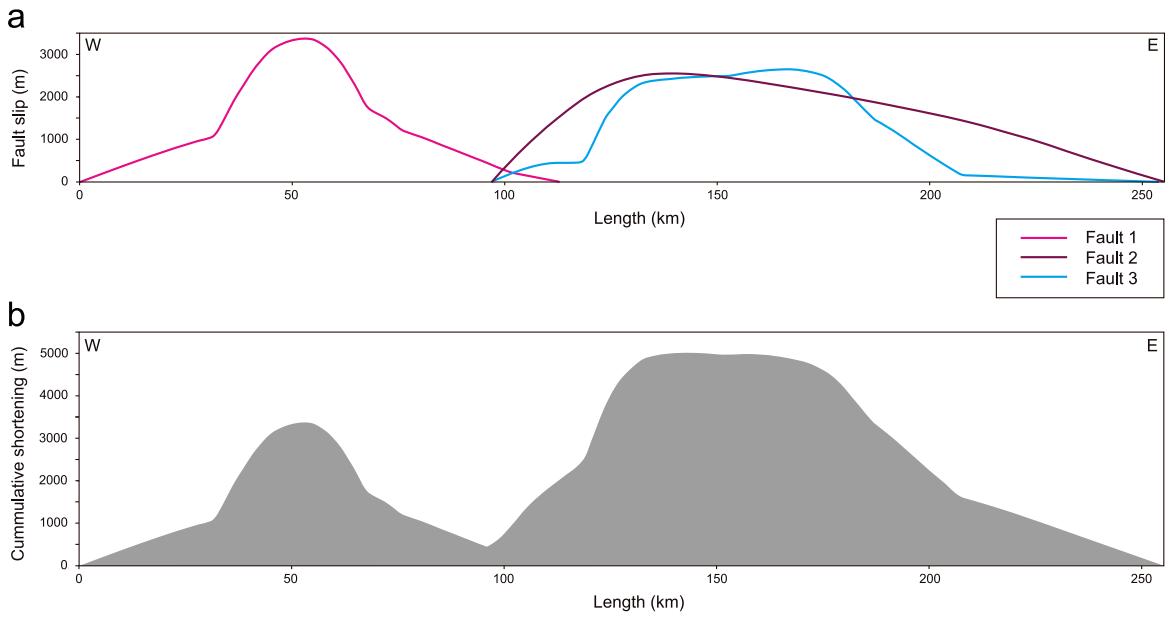

Fig. 6. (a) South Thaumasia faults slip distribution. (b) Cumulative horizontal shortening.

faults (labeled as faults 4 and 5) that partially overlap each other (Fig. 7). Both faults show associated propagation asymmetric anticlines indicating a SE vergence. A set of sub-parallel wrinkle ridges is present on the footwall (southern fault block).

The 3D retrodeformation of the observed topography (Fig. 8a) performed with the aim of eliminating the topographic effect of the contractional structures (Fig. 8b) provided us a first approximation to the fault geometries and slip distribution. We produced a surface free of craters and contractional structures (Fig. 8c) to be used as an initial topography for the forward modeling. The final modeled surface (Fig. 8d) successfully reproduces the observed topography (Fig. 8a) of the studied contractional structures. The largest misfit values between the observed and modeled topography (Fig. 9) correspond to impact craters which were not reproduced during tectonic modeling. Consequently, the numerical calculation of the difference between the observed topography (Fig. 8a) and the forward modeled topography (Fig. 8d) has been made excluding crater values. The median value of the error is ~ -2 m. The quartile deviation associated with this median value, which is indicative of the average fit of the model, is ~27 m, indicating that half of the values obtained when comparing these two surfaces are concentrated between +25 and −29 m.

The resultant geometry for both modeled faults is characterized by an upper planar shape dipping ~33° that roots with a listric geometry into a 16–19 km deep decollement level (Fig. 10, Table 1). Although both faults seem to root at the same depth, their slips are very different. Fault 4 shows a maximum slip of 801 m while Fault 5 provides a maximum slip of 2847m. In this fault system, the shorter Fault 5 (90 km) accommodates more than 3 times as much shortening as the larger Fault 4 (157 km). The classical fault slip distribution obtained from the forward modeling is shown for each fault in Fig. 11a, which is characterized by an overall symmetrical distribution with a maximum in the central zone and a gradual decay toward the lateral tips. The cumulative shortening (horizontal slip) is shown by Fig. 11b. The maximum is located toward the NE of the fault complex since Fault 5 generated a higher contraction. The trishear angles used to reproduce the shape of the fault propagating fold were 85-89°, with an associated propagation to slip ratio of 3 and tip points starting at −4000 to 0 m of elevation.

4. Discussion

The large thrust faults modeled here are among the most prominent features generated by tectonic contraction of the Martian lithosphere. The study of these faults and associated folds gives us information about how tectonic contraction took place in the frontal thrust of Thaumasia Montes and how it was transmitted toward the south in Aonia Terra, providing insights into the Martian lithospheric and crustal structure, thermal state and evolution in this area.

4.1. Vergence of the thrust fault system

The vergence of the thrust fault system concentric to Tharsis was studied by Okubo and Schultz (2003) through the asymmetry of the fault-propagation folds by the analysis of topographic profiles radial to Tharsis. They found that the frequency of thrust faults with outward vergence was equal to the frequency of structures with the opposite vergence, concluding that the hypothesis of a common detachment level of faulting for these structures should be rejected. Contrasting with this result, all the detailed tectonic studies performed on specific structures

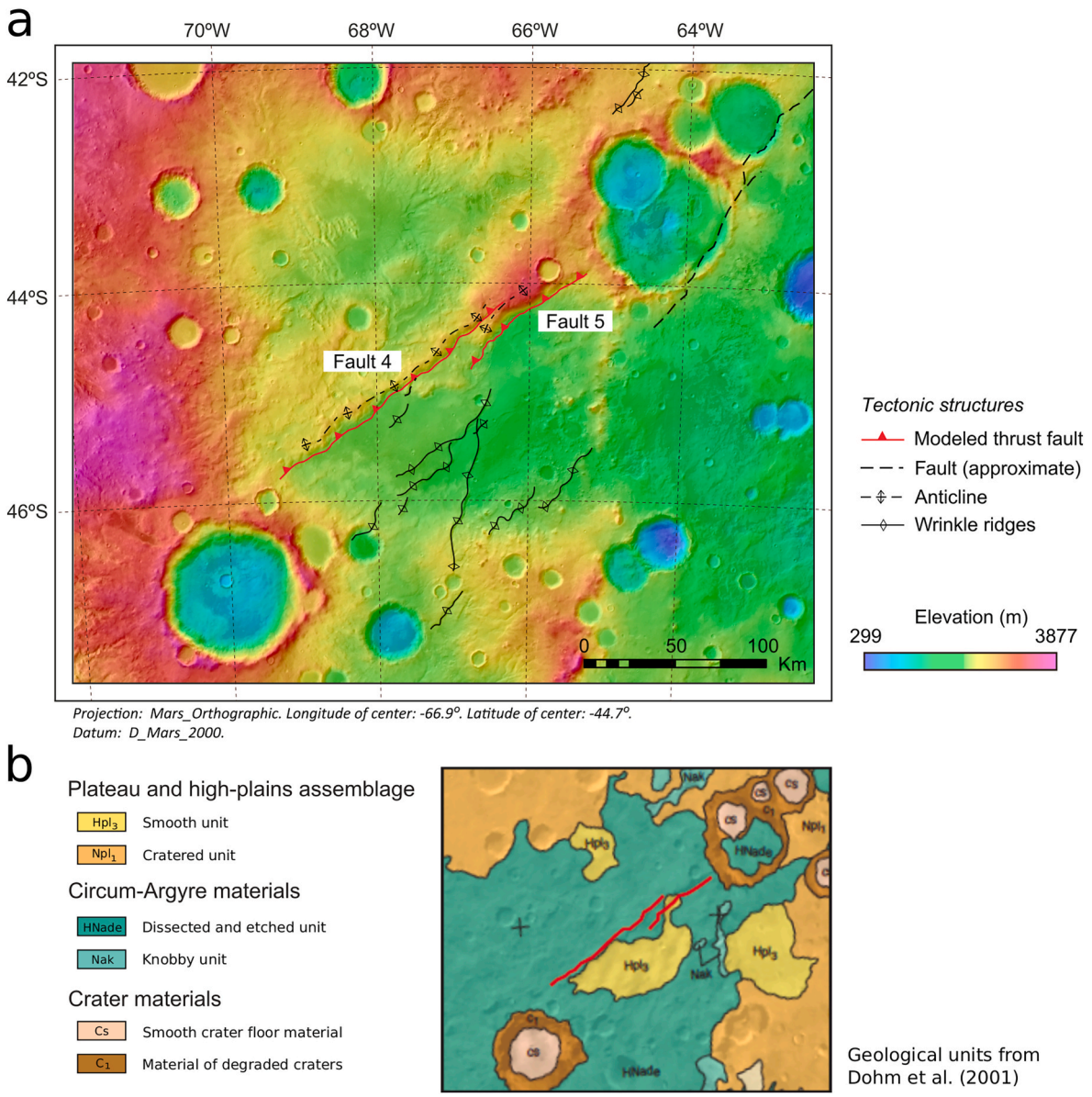

Fig. 7. (a) Structural map of the modeled thrust faults in Phrixi Rupes. The base map is made by combining a MOLA model (DEM) over a THEMIS-IR Day image. The modeled large thrust faults are labeled and marked in red. The fault-propagation anticlines generated on the hanging wall of every modeled thrust are mapped. Other minor faults and wrinkle ridges colored in black were not included in the models. (b) Geological units of the same area from Dohm et al. (2001), the traces of the studied faults are marked in red. (For interpretation of the references to color in this figure legend, the reader is referred to the Web version of this article.)

in the study area show a radial outwards vergence with respect to Thaumasia Montes and, therefore, to the Tharsis bulge. An outward vergence of the thrust frontal system bounding Thaumasia Montes toward the south and southwest was also found by the regional studies of Anguita et al. (2006) and Borraccini et al. (2007). A more detailed analysis of the South Thaumasia thrust system was made by Grott et al. (2007) and Ruiz et al. (2009) pointing out a southwards vergence of the faults, indicating that Thaumasia Montes is thrusting on the southern terrains. Similarly, the outer thrust system arc parallel to Thaumasia boundary formed by Phrixi, Ogygis and Bosporos Rupes has been studied with different structural techniques showing a south to southwest vergence (Herrero-Gil et al., 2019; Herrero-Gil., 2020a). An equivalent out-of-Tharsis vergence was described by Klimczak et al. (2018) for Icaria, Phrixi, Bosporos and Ogygis Rupes, surrounding the Tharsis bulge with an arc geometry from the southwest, the south and the southeast. Moreover, the detailed 3D structural modeling shown here confirms the southward vergence of the three modeled faults of the South Thaumasia thrust fault system (Fig. 2) together with the two faults of Phrixi Rupes (Fig. 7). Although none of the studied areas in this contribution present thrust faults verging opposite to the general out-of-Tharsis trend, there are some subsidiary backthrusts in the nearby structures. Ogygis Rupes presents two minor subsidiary backthrusts with a NW vergence but their cumulative displacement is significantly smaller that Ogygis main fault with a SE vergence (Herrero-Gil et al., 2020a). Similarly, Bosporos Rupes shows a large parallel backthrust providing a general pop-up geometry, but the displacement indicated by the topographic signature of the SE-vergent Bosporos Rupes is significantly higher than the displacement of the NW-vergent backthrust (Herrero-Gil et al., 2019). This could explain the apparent discrepancy between the observation of a similar frequency of inward and outward of Tharsis vergence in the compressional structures reported by Okubo and Schultz (2003) and the dominant outward of Tharsis vergence in the south to southeast boundary of Thaumasia described by Anguita et al. (2006), Borraccini et al. (2007), Grott et al. (2007), Ruiz et al. (2009),

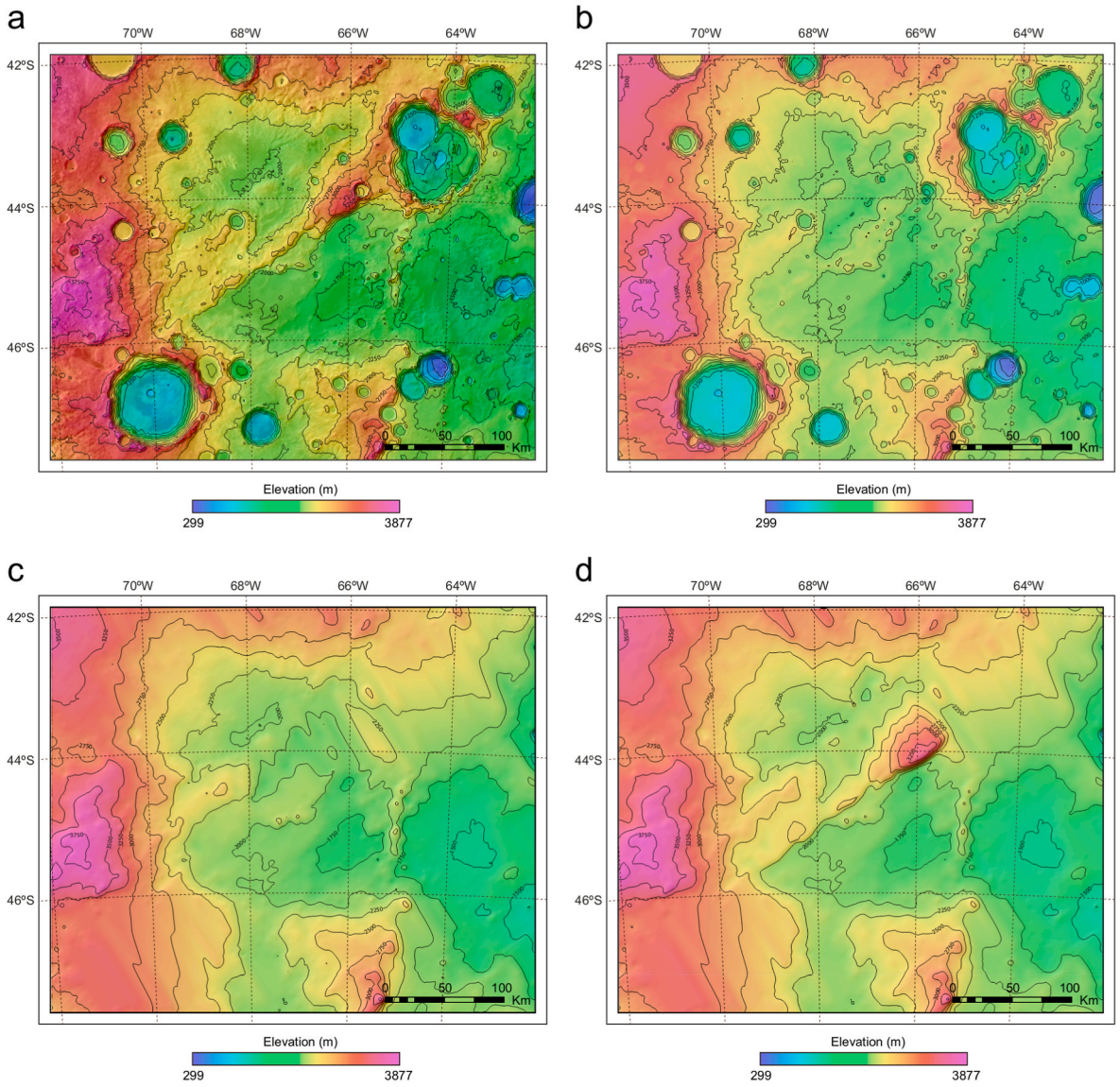

Fig. 8. Digital elevation models used and obtained during the modeling of Phrixi Rupes. a) Observed MOLA topography. b) Restored digital elevation model after the retrodeformation of the two modeled faults. c) Smooth digital elevation model where the relief caused by faults and impact craters has been removed (this topography was used as the starting stage for the 3D forward modeling). d) Digital elevation model obtained at the end of the forward modeling reproducing the main relief signatures associated with the faults observed in (a).

Klimczak et al. (2018) and Herrero-Gil et al. (2019, 2020a). Indeed, Okubo and Schultz (2003) computed all the structures without considering the displacement accommodated by each specific structure and they found no dominant vergence, but when the most prominent structures are studied in detail, each one shows, without exception, an out-of-Tharsis vergence. Moreover, this downslope vergence is the dominant tectonic transport direction expected when contraction took place between the thickened crust of the Tharsis bulge and the lower surrounding terrains of Aonia Terra.

Beyond the area studied in the present work, a detailed structural modeling of wrinkle ridges observed at Lunae Planun (Karagoz et al., 2022) shows an out-of-Tharsis vergence, and, at least in this location, the regular spacing of the thrusts suggests the presence of a common detachment level providing an orogenic wedge geometry. Similarly, an out-of-Tharsis vergence toward the east can be found in the Coprates Rise thrust fault system (Schultz and Tanaka, 1994), at the eastern boundary of the Thaumasia Montes.

4.2. *Presence or absence of a common detachment level*

Geodynamic models of the lithospheric structure of the Tharsis bulge and the surrounding terrains have been the subject of discussion between detached or welded models at the base of the Tharsis volcanic pile. A detached Tharsis crust due to a ductile behavior in the lower crust was proposed by Tanaka et al. (1991) based on observations of the distribution of radial graben. The non-dominant vergence of the concentric contractional structures found by Okubo and Schultz (2003) favored a model where the Tharsis crust is welded to the mantle with a common brittle behavior.

The regular spacing of thrust faults and associated propagation folds in orogenic belts on Earth has been considered as evidence of the presence of a common detachment level (e.g., Morley et al., 2011; Goff et al., 1996; Ruh et al., 2012). This is not the case for the studied faults presented here. The shortening accommodated by thrust faults on Mars, including lobate scarps and wrinkle ridges, was calculated to range from 0.007% to 0.13% over the Hesperian (Nahm and Schultz, 2011), based on the fault inventory performed by Knapmeyer et al. (2006, 2008),

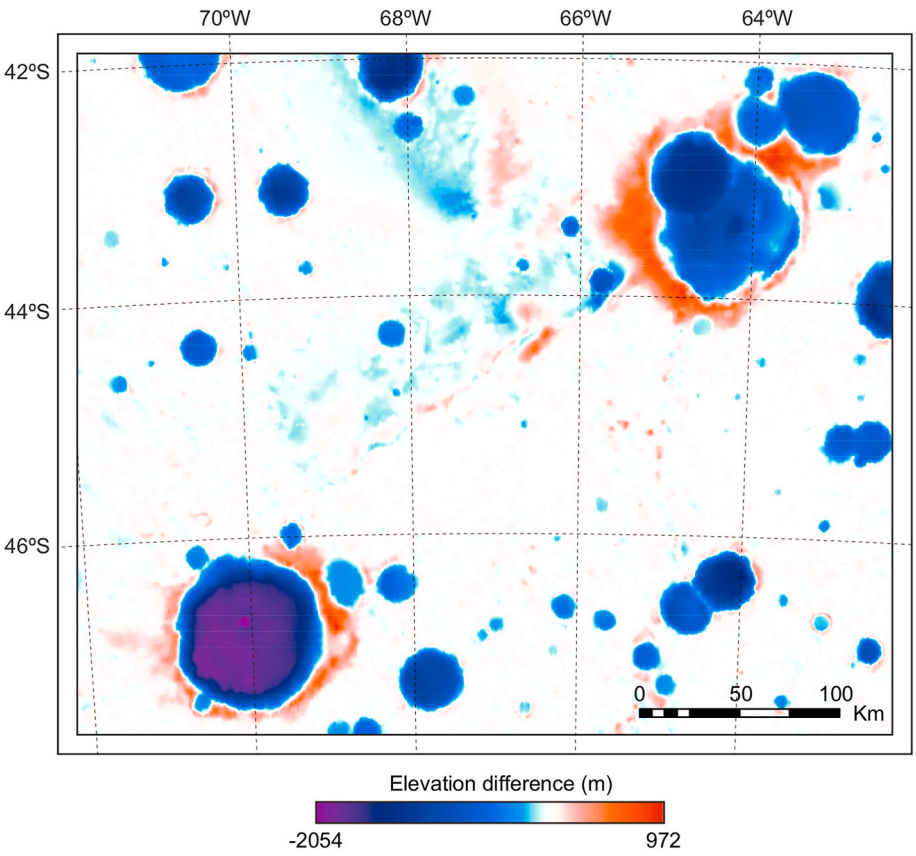

Fig. 9. Misfit of the 3D forward modeled topography with the observed MOLA topography for Phrixi Rupes. Cero values are shown in white color indicating a good fit. Note that the main error sources came from impact cratering that was not reproduced during forward modeling. (For interpretation of the references to color in this figure legend, the reader is referred to the Web version of this article.)

which are contraction values similar to intraplate deformations on Earth (e.g. Schultz, 2003; Klimczak et al., 2019). The relative scarcity of prominent contractional structures (lobate scarps) on Mars due to small amounts of shortening preclude the formation of regular spacing controlled by the presence of a possible detachment at depth, thus the regular or non-regular spatial distribution of large contractional structures cannot be used as an indicator of the presence of a common level of detachment in Mars. Moreover, analogue modeling has shown that the presence of viscous material in the detachment, together with slow convergence rates, favors a symmetric distribution of thrust vergences in collisional orogens (e.g., Luján et al., 2006).

Nevertheless, the obtained 3D models for the South Thaumasia faults (Fig. 5) and Phrixi Rupes (Fig. 10), together with the 3D model of Ogygis Rupes (Herrero-Gil et al., 2020a) show that all the studied faults share a similar geometry, being planar for the first kilometers and listric at depth. The reconstruction of this deep listric geometry is controlled by the morphology of the backlimb (Herrero-Gil et al., 2020a, 2020b). If the thrust faults were completely planar, keeping their dips constant and abruptly ending at depth, this necessarily would imply that the flow of the hanging wall material changes abruptly from a horizontal movement to a fault-parallel movement at a Kink-type synform plane. In that case, the fault-parallel flow of the hanging wall would generate a backlimb with a constant dip parallel to the fault dip and sharp limits (e.g., Amos et al., 2007; Brandemburg, 2013; Hardy and Ford, 1997). This kind of backlimb is not present in any of the studied faults, conversely, their backlimbs are characterized by smooth variations of slope in their limits, which, when using the fault-parallel flow algorithm for the deformation of the hanging wall, implies a listric fault geometry at depth.

The chosen modeling method highly conditions our vision of the geometry of the modeled faults. The large Martian thrust faults were frequently modeled by the forward displacement of a blind dislocation plane into an elastic medium (Shultz and Watters, 2001; Grott et al., 2007; Ruiz et al., 2008; Egea-González et al., 2017; Herrero-Gil et al., 2019). This method was also successfully applied to large thrust faults of other planetary bodies (e.g. Watters et al., 2002, 2011; Egea-González et al., 2012; Williams et al., 2013). The forward mechanical dislocation method has favored a simple vision of thrust faults as constant dip planes. Although this modeling method successfully reproduces the general characteristics of the topography of fault-propagation folds, it necessarily assumes that the thrust fault does not break the surface (the upper fault tip is located at the topographic surface or bellow). The models that locate the upper tip point exactly at the topographic surface do not break that surface, i.e. there is no displacement or rupture of the topographic surface, thus the topographic surface suffers pure elastic deformation. The models that locate the upper fault tip below the topographic surface maintain a continuum rock elastic media intact above the upper fault tip during all the fault displacement, providing the high slope of the anticline frontal limb. It is well known that this assumption does not hold for any of the main faults underlying lobate scarps on Mars or other rocky planetary bodies. The evolution of faulting with an upwards propagation ends, for the largest thrust faults, with the fault clearly breaking the topographic surface, therefore generating a trace of surface rupture at the base of the frontal limb of the fault-propagation fold. The rupture lengths of the main thrust faults on Mars were measured by Klimczak et al. (2018), including all the lobate scarps modeled in this study. The forward mechanical dislocation modeling usually considers a decrease of slip toward the fault tip points, including the lower tip. This procedure helps to reproduce the gradual variation of topography at the backlimb. This decrease of slip at the bottom of the modeled planar fault was interpreted by Herrero-Gil et al. (2019) as an evidence of the fault entering a wide detachment level interpreted to be the brittle-ductile transition (BDT). The inclusion of

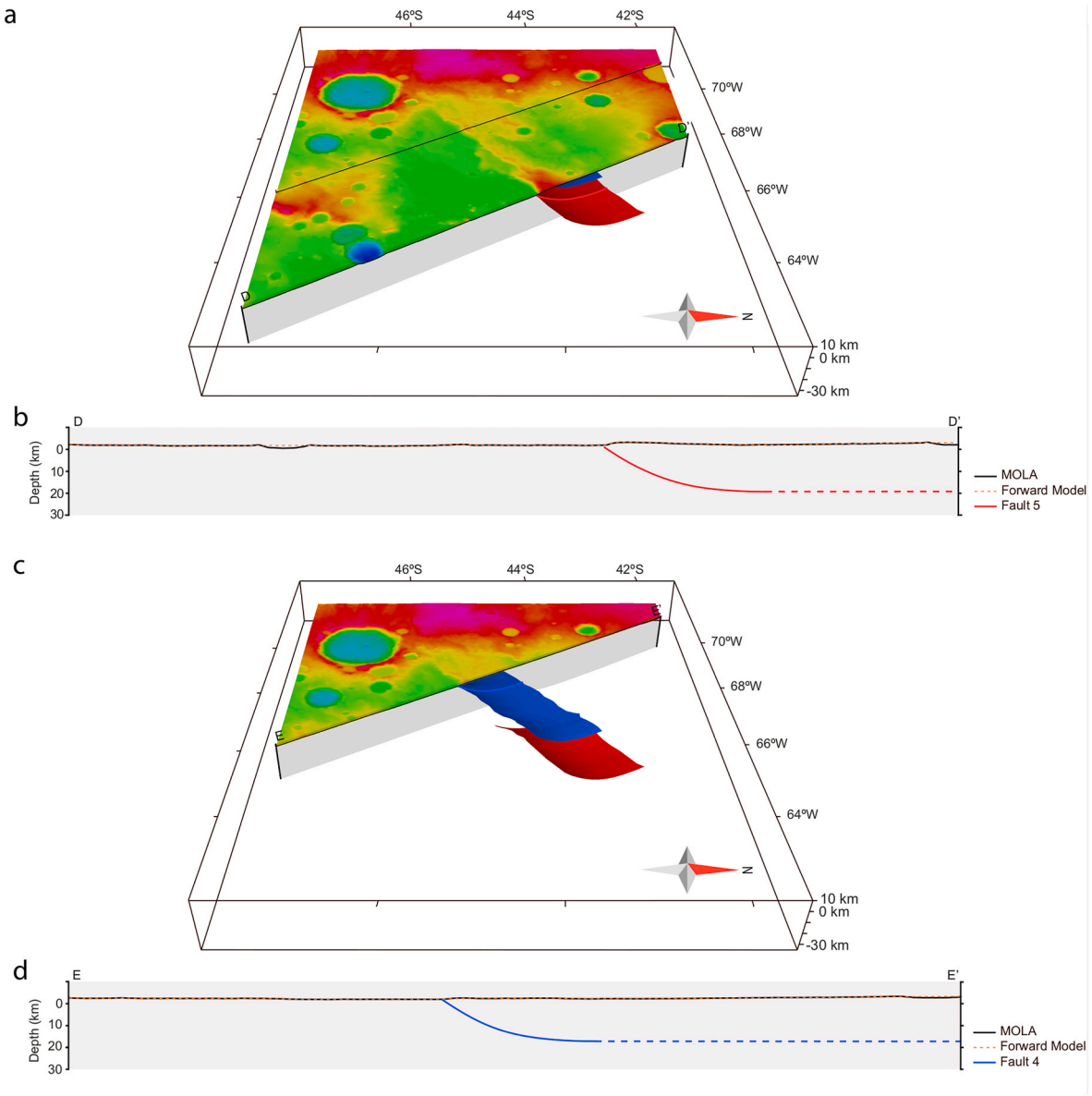

Fig. 10. Phrixi Rupes modeled fault geometries. (a) Perspective of the 3D model of Phrixi Rupes faults where MOLA topographic surface has been hidden northeast of D-D′ to show the underlying plane of Fault 5. (b) Cross Section D-D′ perpendicular to the mean strike of the faults showing a listric geometry at depth for Fault 5. (c) Perspective of the 3D model of the Phrixi Rupes faults where MOLA topographic surface has been hidden northeast of E-E′ to show the underlying planes of Faults 4 and 5. (d) Cross Section E-E′ perpendicular to the mean strike of the faults showing a listric geometry at depth for Fault 4.

this slip variation in the bottom tip of the forward mechanical dislocation modeling generates a similar topographic effect as the inclusion of a basal listric fault zone in our 3D modeling, which also we interpret as the rooting of the fault into a detachment level.

4.3. Architecture of the thrust system

There is a key difference between the nature of the South Thaumasia Faults and the faults of Aonia Terra (Ogygis, Phrixi and Bosporos Rupes). The former were developed between two distinct units with different surface ages (Early Noachian Thaumasia Montes at the hanging wall to the north, and Early Hesperian smooth units at the footwall to the south), while the latter were developed exclusively in the Late Noachian-Early Hesperian units of Aonia Terra (ages are supported by crater densities from Dohm and Tanaka, 1999; Dohm et al., 2001). Therefore, the observed topographic signature of the South Thaumasia faults does not represent the total fault displacement, since the fault-propagation anticline and the fault scarp were already present when the Early Hesperian Aonia Terra units were emplaced, somewhat reducing the observed topographic effect of Faults 1 and 2. Thus, the obtained modeled slip is a minimum estimate for the South Thaumasia Thrust faults, although they already present the largest cumulative slip. The shortening accommodated by this fault system in a narrow deformation belt between Thaumasia Montes and the surrounding units of Aonia Terra toward the south is responsible of the elevation by thrusting of the Thaumasia block over the Southern Aonia Terra terrains. From this point of view, the South Thaumasia faults act as a backstop-like structure for a distributed incipient wedge of contractional structures propagated into Aonia Terra between the Thaumasia block and the Argyre impact basin (including Phrixi, Ogygis and Bosporos among other minor structures). The larger depths of faulting reached by the South Thaumasia faults (up to 27.5 km) interpreted to represent a backstop with respect to the depth of faulting of Aonia Terra thrusts (~17 km for Ogygis, and 16–19 km for Phrixi), together with the

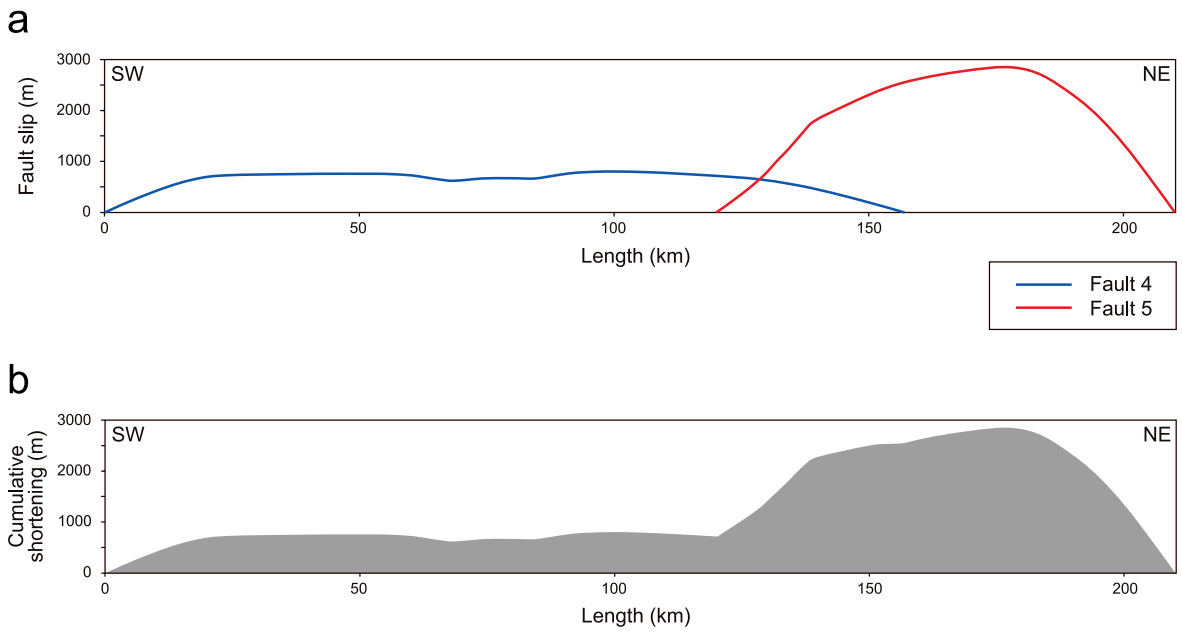

Fig. 11. (a) Phrixi Rupes faults slip distribution. (b) Cumulative horizontal shortening.

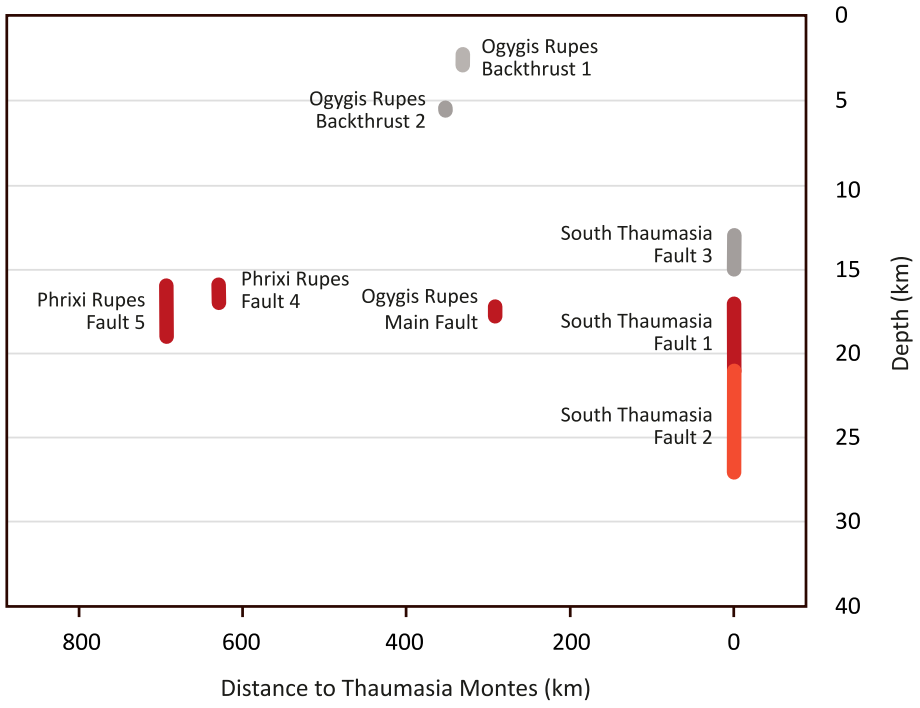

Fig. 12. Spatial distribution of the depth of faulting obtained in this study for the South Thaumasia Faults and Phrixi Rupes and the results of the modeled faults obtained by the same method for Ogygis Rupes (Herrero-Gil et la., 2020a). Note that the depth of faulting of the main faults becomes shallower away from Thaumasia.

discussed evidence of a common detachment level, provide evidence for a contractional wedge interpretation (Fig. 12).

The depth of faulting of Bosporos Rupes, estimated to be 45 km by the balanced cross section method and 33–41 km by Forward Dislocation modeling (Herrero-Gil et al., 2019), lies out of the general trend of a shallower depth of faulting outwards of Tharsis (Fig. 12). Bosporos Rupes is the only lobate scarp of the study area that was nucleated on an Argyre impact basin ring. For this reason, probably, the tectonic uplift and consequently the depth of faulting for Bosporos Rupes was overestimated in that study, since the contribution to the topography of the displacement of Bosporos thrust and the Argyre rim VI (as defined by Heisinger and Head, 2002) cannot be discerned.

The shortening accomplished by the studied thrust fault system is very small compared to contractional wedges of thrust and fold belts on Earth. The lateral expansion of the Tharsis bulge generates a distributed deformation belt surrounding the Thaumasia uplifted block accommodated by scarce large thrust faults with an outwards vergence, together with few minor backthrusts and other subsidiary faults. A distributed contraction in the blocks between the main faults is evidenced by the generation of wrinkle ridges indicating a brittle contractional

deformation of the upper units.

An incipient thrust wedge architecture is outlined by the general out-of-Tharsis vergence, the listric fault geometries and the deepening of the depth of faulting toward Thaumasia. Nevertheless, the moderate amount of shortening (several km) precludes the thrust system to reach a critical taper wedge geometry in gravitational equilibrium like the orgenic wedges on Earth characterized by large values of horizontal shortening (hundreds of kilometers). This is in good agreement with the results of Nahm and Schultz (2010), who applied the theory of critical taper wedge mechanics to the Thaumasia Highlands and found that a critical taper wedge geometry was not reached in this area.

4.4. The thermal state of the crust and the depth to the BDT

The depth of large faults penetrating down until the BDT depth can be used to estimate the surface heat flow at the time of faulting following the method described by Ruiz et al. (2011) and Egea-González et al. (2017). This kind of analysis can give some additional information regarding if the detachment level(s) associated with the South Thaumasia Faults 1 and 2 might be reliably related to the BDT depth.

Faults occur in the cold upper layer of the crust, where brittle deformation prevails. The critical stress difference that is necessary to cause faulting in the brittle lithosphere is given by (e.g., Ranalli, 1997)

$$(\sigma_1 - \sigma_3)_b = \alpha \rho g z (1 - \lambda), \quad (1)$$

where λ is the pore fluid pressure, ρ is the density, g is the acceleration due to the gravity (3.72 m s^{-2}), and z is the depth. The coefficient α depends on the stress regime and takes a value of 3 in the case of thrust faulting (e.g., Ranalli, 1997).

At greater depths, temperature increases and rocks have a ductile behavior under stress. In the ductile regime, the stress differences needed to have a steady-state strain rate $\acute{\epsilon}$ is given by (e.g., Ranalli, 1997)

$$(\sigma_1 - \sigma_3)_d = \left(\frac{\acute{\epsilon}}{A}\right)^{\frac{1}{n}} exp\left(\frac{Q}{nRT}\right), \quad (2)$$

where A and n are laboratory-determined constants, Q is the activation energy of creep, R is the gas constant (8.3145 J mol^{-1} K^{-1}), and T is the absolute temperature. At the brittle-ductile transition depth (Z_{BDT}), brittle and ductile strengths are equal and the temperature at this depth (T_{BDT}) can be calculated from:

$$T_{BDT} = \frac{Q}{nR}\left[ln\left(\frac{(1-\lambda)\alpha\rho g Z_{BDT}}{(\acute{\epsilon}/A)^{1/2}}\right)\right]^{-1}. \quad (3)$$

Thrust faults associated with lobate scarps are thought to cross the crust down to the brittle-ductile transition depth (e.g., Schultz and Watters, 2001; Watters et al., 2002). Thus, the depths of faulting obtained in the previous section from Faults 1 and 2 (17–27 km) allow to calculate T_{BDT}. These faults are the most likely to grow to the brittle-ductile transition.

Pore fluid pressure in the crust is unknown, and therefore we have assumed a pore fluid pressure interval between 0 and 0.35, which are the values for dry and hydrostatic conditions. The rest of parameters used in our calculations are based on values previously considered for Mars (Ruiz et al., 2011; Egea-González et al., 2017); the strain rate ranges between 10^{-16} s^{-1} and 10^{-19} s^{-1} (McGovern et al., 2002; Ruiz et al., 2011), the density for the Martian crust is assumed to be 2900 kg m^{-3} (McGovern et al., 2002; Wieczorek et al., 2022), and we consider creep parameters appropriate for wet diabase: A = 0.0612 MPa^{-n} s^{-1}, n = 3.05 and Q = 276 kJ mol^{-1} (Caristan, 1982).

The so-obtained estimations of the temperature at the BDT can be used to calculate the surface heat flow through (e.g., Ruiz et al., 2008; Egea-González et al., 2017)

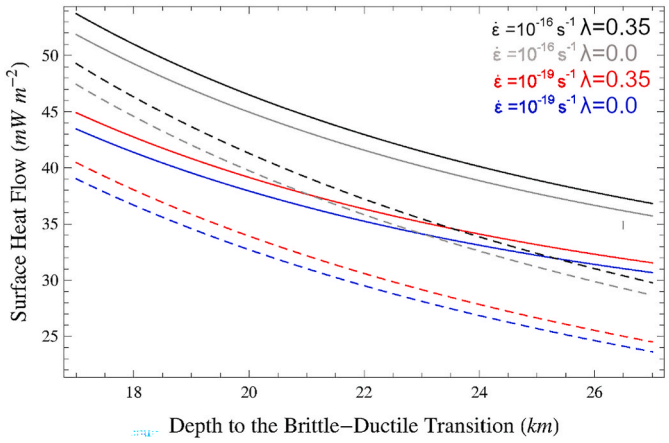

Fig. 13. Surface heat flow as a function of the depth to the brittle–ductile transition, crustal heat sources, strain rate and pore fluid pressure. Solid lines are surface heat flows calculated for sources homogeneously distributed; dashed lines are heat flows calculating for heat sources not included in the calculations (the results are roughly equivalent to heat flow below an upper enriched crust).

$$F_S = \frac{k(T_{BDT} - T_S)}{Z_{BDT}} + \frac{Z_{BDT}H}{2}; \quad (4)$$

where T_S is the temperature at the surface, k is the thermal conductivity of the layer, and H is the volumetric heat production rate in the crust due to radioactive heat sources. We have assumed a thermal conductivity of 2 W m^{-1} K^{-1}, which is appropriated for basaltic rocks (Beardsmore and Cull, 2001), and a surface temperature of 220 K (e.g., Kieffer et al., 1977). Hahn et al. (2011) reported an average heat production of 4.9 × 10^{-11} W kg^{-1} for the average Martian surface. We consider this value as representative of the whole crust (Egea-González et al., 2022), which leads to a heat production at time of faulting of 1.8 × 10^{-10} W kg^{-1} (equivalent to a volumetric heating rate 0.522 × 10^{-7} W m^{-3}) by assuming that the fault system was formed at 3.7 Ga; we have also considered the case without crustal heat sources.

The two extreme scenarios for the presence and distribution of crustal heat sources here explored are useful for our purpose. The case for heat sources homogeneously distributed in the crust is useful for obtained heat flow upper limits, since it would put an upper limit to the radioactive production in the crust. There is evidence for a stratified crust in the Thaumasia highlands (Ruiz et al., 2009), and InSight has obtained some information on the stratification of the crust at the landing site (Wieczorek et al., 2022), but the structure of the highland crust is mostly unknown. In this sense, the surface heat flows without taking into account crustal heat sources are lower limits, but they would be a good approximation for the heat flow below a potential upper enriched crust.

Our calculation yields surface heat flows that range between 24 and 54 mW m^{-2}, depending on BDT depth, strain rate, pore fluid pressure, and inclusion or not of crustal heat sources (Fig. 13). These values partially match the surface flows calculated by Grott et al. (2007) and Ruiz et al. (2009, 2011), which range between 20 and 25 and ~45 mW m^{-2} for the same area. However, our results are somewhat higher due to that we here consider a range of faulting depths including lower values than previous work, as a consequence of the lower faulting depth deduced for the South Thaumasia Fault 1 from the 3D modeling results.

Further constraints to the regional thermal state can be derived by considering the crustal thickness in the Thaumasia highlands, which would be ~91 km for the preferred, density-constant updated crustal models by Wieczorek et al. (2022). On one hand, for the crustal heat production value used here, the radioactive production of a 91 km homogeneous crust provides a surface heat flow of 47 mW m^{-2}; lower

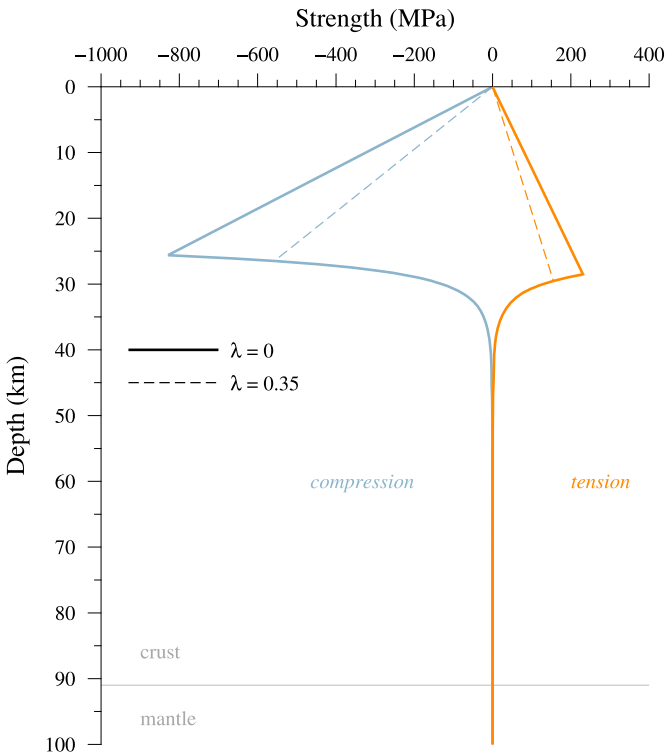

Fig. 14. Strength envelopes for the Thaumasia highlands for a lower crust heat flow of 25 mW m^{-2}, a strain rate of 10^{-19} s^{-1}, and pore fluid pressure for both dry and wet hydrostatic conditions. The heat flow would be equivalent to the heat flow below an upper enriched crust. We used a local crustal thickness of ~91 km, obtained from the uniform crustal density model of Wieczorek et al. (2022).

surface heat flows would imply negative subcrustal heat flow; this problem is even more appealing if inferences for a higher heat production based on InSight data (Khan et al., 2021) are considered. On the other hand, the temperature of the dry basalt solidus in the base of a 91 km thick crust is ≈ 1400 K (Ruiz et al., 2019). This temperature would be reached in the crust for heat flows higher than 50 mW m^{-2} (taking into account crustal heat sources), or higher than 26 mW m^{-2} (without crustal heat sources); this implies that large scale melting would initiate at the base of the Thaumasia highland crust, and the start of melting would occur for lower heat flows for a wet crust.

Thus, there is only a very narrow set of parameters for which we might have realistic results, which help to constraint the actual BDT depth at the time when the thrusts were formed. For the case with crustal heat sources homogeneously distributed, heat flows between 47 and 50 mW m^{-2} can only be obtained for BDT depths of 17–20 km and fast strain rates. For the case without heat sources, calculated heat flows between 24 and 26 mW m^{-2} (roughly equivalent to the heat flow below an upper enriched crust) can only be obtained for BDT depths of 25–27 km and slow strain rates.

Our results therefore favor a crustal BDT depth of ~25 km in the Thaumasia highlands. Indeed, a BDT depth of at most ~20 km would require a very homogeneous crust, which is not supported by previous work on this zone; moreover, slow strain rates of 10^{-19} s^{-1} or similar are consistent with contraction linked to lithosphere cooling (e.g., Kumar and Gordon, 2009). Thus, South Thaumasia Fault 2 is probably rooted at the BDT, whereas South Thaumasia Fault 1 most probably was related to a mechanical discontinuity inside the brittle crust. Fig. 14 shows strength envelopes for dry and wet conditions representatives of the studied area, and including both compression and tension stress regimes for completeness. It can be seen that all the strength of the lithosphere is located in the upper half of the crust, without significant contributions from the lower crust or the upper mantle.

5. Conclusions

The detailed geometry at depth, together with the complexities of the slip distributions and fault-propagation folding of the South Thaumasia thrust faults and Phrixi Rupes have been obtained through a 3D modeling technique based on the fault-parallel flow of the hanging wall and the trishear algorithms to model the associated fault-propagation folding. The observed general out-of-Tharsis vergence of the studied structures and other main thrust faults in the area (Ogygis Rupes and Bosporos Rupes), the upper planar fault geometries changing to listric at depth and the general trend of a shallower depth of faulting to the south and southeast, suggest that this thrust system presents a wedge geometry with a common detachment level being pushed by the raised Thaumasia basement block thrusting over the Aonia Terra units. Nevertheless, the small amount of shortening prevents the system to develop a critical taper wedge geometry in gravitational equilibrium like terrestrial orogenic wedges. Using the depth of faulting of the largest structures as an indicator for the depth of the BDT, the heat flows at the time of formation range between 24 and 54 mW m^{-2}. The obtained strength envelopes for dry and wet conditions indicate that the strength of the lithosphere was mainly located in the BDT and the brittle domain of the lithosphere (corresponding to the upper crust) at the time of faulting.

Declaration of competing interest

The authors declare that they have no known competing financial interests or personal relationships that could have appeared to influence the work reported in this paper.

Data availability

Data will be made available on request.

Acknowledgments

This research has been supported by the project TECTOMARS PGC2018-095340-B-I00, funded by the Spanish Ministry of Science, Innovation and Universities. The software MOVE 2019.1 was provided by Petroleum Experts Ltd. through the donation of an Academic license to the Departamento de Geodinámica, Estratigrafía y Paleontología, Universidad Complutense de Madrid. The data used in this research are available online at the NASA Planetary Data System. We would like to thank Chris Okubo and an anonymous reviewer for their encouraging and thorough reviews, which greatly improved the quality of this article.

References

Andrews-Hanna, J.C., Broquet, A., 2023. The history of global strain and geodynamics on Mars. Icarus 395, 115476. https://doi.org/10.1016/j.icarus.2023.115476.
Amos, C.B., Burbank, D.W., Nobes, D.C., Read, S.A., 2007. Geomorphic constraints on listric thrust faulting: implications for active deformation in the Mackenzie Basin, South Island, New Zealand. J. Geophys. Res. 112, B03S11.
Anguita, F., Fernández, C., Cordero, G., Carrasquilla, S., Anguita, J., Núñez, A., et al., 2006. Evidences for a Noachian-Hesperian orogeny in Mars. Icarus 185, 331–357.
Allmendinger, R., 1998. Inverse and forward numerical modeling of trishear fault-propagation folds. Tectonics 17 (4), 640–656.
Arizona State University (ASU), 2010. THEMIS Day IR 100m global mosaic. http://www.mars.asu.edu/data/thm_dir_100m/.
Atkins, R.M., Byrne, P.K., Bohnenstiehl, D.R., Wegmann, K.W., 2022. A morphometric investigation of large-scale crustal shortening on Mars. J. Geophys. Res.: Planets 127, e2021JE007110. https://doi.org/10.1029/2021JE007110.
Beardsmore, G.R., Cull, J.P., 2001. Crustal Heat Flow: a Guide to Measurement and Modelling. Cambridge university press.
Borraccini, F., Di Achille, G., Ori, G.G., Wezel, F.C., 2007. Tectonic evolution of the eastern margin of the Thaumasia Plateau (Mars) as inferred from detailed structural mapping and analysis. J. Geophys. Res.: Planets 112, E05005. https://doi.org/10.1029/2006JE002866.
Brandemburg, J.P., 2013. Trishear for curved faults. J. Struct. Geol. 53, 80–94.

Carr, M.H., Head III, J.W., 2010. Geologic history of Mars. Earth Planet Sci. Lett. 294 (3–4), 185–203.
Caristan, Y., 1982. The transition from high temperature creep to fracture in Maryland diabase. J. Geophys. Res. Solid Earth 87 (B8), 6781–6790.
Chicarro, A.F., Schultz, P.H., Masson, P., 1985. Global and regional ridge patterns on Mars. Icarus 63 (1), 153–174. https://doi.org/10.1016/0019-1035(85)90025-9.
Christensen, P., Jakosky, B.M., Kieffer, H.H., Malin, M.C., McSween Jr., H.Y., Nealson, K., et al., 2004. The thermal emission imaging system (THEMIS) for the Mars 2001 Odyssey mission. Space Sci. Rev. 110, 85–130.
Dohm, J.M., Tanaka, K.L., 1999. Geology of the Thaumasia region, Mars: plateau development, valley origins, and magmatic evolution. Planet. Space Sci. 47 (3–4), 411–431.
Dohm, J.M., Tanaka, K.L., Hare, T.M., 2001. Geologic map of the Thaumasia region of Mars. Assemblage 2 (5), 16. U.S. Geological Survey Geologic Investigations Series I–2650, 3 sheets. https://pubs.usgs.gov/imap/i2650/.
Edwards, C.S., Nowicki, K.J., Christensen, P.R., Hill, J., Gorelick, N., Murray, K., 2011. Mosaicking of global planetary image datasets: 1. Techniques and data processing for Thermal Emission Imaging System (THEMIS) multi-spectral data. J. Geophys. Res. 116, E10008 https://doi.org/10.1029/2010JE003755.
Egan, S.S., Buddin, T.S., Kane, S.J., Williams, G.D., 1997. Three-dimensional modelling and visualization in structural geology: new techniques for the restoration and balancing of volumes. Proceedings of the 1996 Geoscience Information Group Conference on Geological Visualization. Electronic Geology 1, 67–82.
Egea-González, I., Ruiz, J., Fernández, C., Williams, J.P., Márquez, A., Lara, L.M., 2012. Depth of faulting and ancient heat flows in the Kuiper region of Mercury from lobate scarp topography. Planet. Space Sci. 60, 193–198.
Egea-González, I., Jiménez-Díaz, A., Parro, L.M., Lopez, V., Williams, J.P., Ruiz, J., 2017. Thrust fault modeling and Late-Noachian lithospheric structure of the circum-Hellas region, Mars. Icarus 288, 53–68.
Egea-González, I., Lois, P.C., Jiménez-Díaz, A., Bramson, A.M., Sori, M.M., Tendero-Ventanas, J.Á., et al., 2022. The stability of a liquid-water body below the south polar cap of Mars. Icarus 383, 115073.
Erslev, E.A., 1991. Trishear fault-propagation folding. Geology 19, 617–620.
Goff, D.F., Wiltschko, D.V., Fletcher, R.C., 1996. Décollement folding as a mechanism for thrust-ramp spacing. J. Geophys. Res. Solid Earth 101 (B5), 11341–11352.
Golombek, M.P., Bridges, N.T., 2000. Erosion rates on Mars and implications for climate change: constraints from the Pathfinder landing site. J. Geophys. Res. 105 (E1), 1841–1853.
Grott, M., Hauber, E., Werner, S.C., Kronberg, P., Neukum, G., 2007. Mechanical modeling of thrust faults in the Thaumasia region, Mars, and implications for the Noachian heat flux. Icarus 186, 517–526.
Hahn, B.C., McLennan, S.M., Klein, E.C., 2011. Martian surface heat production and crustal heat flow from Mars Odyssey Gamma-Ray spectrometry. Geophys. Res. Lett. 38 (14).
Hardy, S., Ford, M., 1997. Numerical modeling of trishear fault propagation folding. Tectonics 16 (5), 841–854.
Hiesinger, H., Head III, J.W., 2002. Topography and morphology of the Argyre Basin, Mars: implications for its geologic and hydrologic history. Planet. Space Sci 50, 939–981.
Herrero-Gil, A., Egea-González, I., Ruiz, J., Romeo, I., 2019. Structural modeling of lobate scarps in the NW margin of Argyre impact basin, Mars. Icarus 319, 367–380.
Herrero-Gil, A., Ruiz, J., Romeo, I., 2020a. 3D modeling of planetary lobate scarps: the case of Ogygis Rupes, Mars. Earth Planet Sci. Lett. 532, 116004.
Herrero-Gil, A., Ruiz, J., Romeo, I., 2020b. Lithospheric contraction on Mars: a 3D model of the Amenthes thrust fault system. J. Geophys. Res.: Planets 125, e2019JE006201. https://doi.org/10.1029/2019JE006201.
Karagoz, O., Kenkmann, T., Wulf, G., 2022. Circum-Tharsis wrinkle ridges at Lunae Planum: morphometry, formation, and crustal implications. Icarus 374, 114808.
Kieffer, H.H., Martin, T.Z., Peterfreund, A.R., Jakosky, B.M., Miner, E.D., Palluconi, F.D., 1977. Thermal and albedo mapping of Mars during the Viking primary mission. J. Geophys. Res. 82 (28), 4249–4291.
Khan, A., et al., 2021. Upper mantle structure of Mars from InSight seismic data. Science 373 (6553), 434–438. https://doi.org/10.1126/science.abf2966.
Klimczak, C., Kling, C.L., Byrne, P.K., 2018. Topographic expressions of large thrust faults on Mars. J. Geophys. Res.: Planets 123, 1973–1995. https://doi.org/10.1029/2017JE005448.
Knapmeyer, M., Oberst, J., Hauber, E., Wählisch, M., Deuchler, C., Wagner, R., 2006. Working models for spatial distribution and level of Mars' seismicity. J. Geophys. Res. 111, E11006.
Knapmeyer, M., Schneider, S., Misun, M., Wählisch, M., Hauber, E., 2008. An extended global inventory of Mars Surface Faults. In: European Geophysical Union General Assembly, vol. 10. European Geophysical Union, Vienna, Austria [abstract].
Kumar, R.R., Gordon, R.G., 2009. Horizontal thermal contraction of oceanic lithosphere: the ultimate limit to the rigid plate approximation. J. Geophys. Res. 114, B01403 https://doi.org/10.1029/2007JB005473.
Luján, M., Storti, F., Rossetti, F., Crespo-Blanc, C., 2006. Extrusion vs. accretion at the frictional-viscous décollement transition in experimental thrust wedges: the role of convergence velocity. Terra. Nova 18, 241–247.
Malin, M.C., Bell III, J.F., Cantor, B.A., Caplinger, M.A., Calvin, W.M., Clancy, R.T., et al., 2007. Context camera investigation on board the Mars reconnaissance orbiter. J. Geophys. Res. 112, E05S04.
McGovern, P.J., Solomon, S.C., 1993. State of stress, faulting, and eruption characteristics of Large Volcanoes on Mars. J. Geophys. Res. 98 (E12), 23.553-23.579.
McGovern, P.J., Solomon, S.C., Smith, D.E., Zuber, M.T., Simons, M., Wieczorek, M.A., et al., 2002. Localized gravity/topography admittance and correlation spectra on Mars: implications for regional and global evolution. J. Geophys. Res.: Planets 107 (E12), 19-1.
Mege, D., Masson, P., 1996. Stress models for Tharsis formation, Mars. Planet. Space Sci. 44 (12), 1471–1497.
Morley, C.K., King, R., Hillis, R., Tingay, M., Backe, G., 2011. Deepwater fold and thrust belt classification, tectonics, structure and hydrocarbon prospectivity: a review. Earth Sci. Rev. 104 (1–3), 41–91.
Nahm, A.L., Schultz, R.A., 2010. Evaluation of the orogenic belt hypothesis for the formation of the Thaumasia Highlands, Mars. J. Geophys. Res.: Planets 115, E04008. https://doi.org/10.1029/2009JE003327.
Nahm, A.L., Schultz, R.A., 2011. Magnitude of global contraction on Mars from analysis of surface faults: implications for Martian thermal history. Icarus 211 (1), 389–400. https://doi.org/10.1016/j.icarus.2010.11.003.
National Aeronautics and Space Administration (NASA), Planetary Data System (PDS), 2014. MOLA digital elevation model global 463 m. https://astrogeology.usgs.gov/search/map/Mars/GlobalSurveyor/MOLA/Mars_MGS_MOLA_DEM_mosaic_global_463m.
Okubo, C.H., Schultz, R.A., 2003. Thrust fault vergence directions on Mars: a foundation for investigating global-scale Tharsis-driven tectonics. Geophys. Res. Lett. 30 (22) https://doi.org/10.1029/2003GL018664.
Ranalli, G., 1997. Rheology of the lithosphere in space and time. Geological Society, London, Special Publications 121 (1), 19–37.
Ruh, J.B., Kaus, B.J., Burg, J.P., 2012. Numerical investigation of deformation mechanics in fold-and-thrust belts: influence of rheology of single and multiple décollements. Tectonics 31 (3). https://doi.org/10.1029/2011TC003047.
Ruiz, J., Fernandez, C., Gomez-Ortiz, D., Dohm, J.M., Lopez, V., Tejero, R., 2008. Ancient heat flow, crustal thickness, and lithospheric mantle rheology in the Amenthes Region, Mars. Earth Planet Sci. Lett. 270, 1–12.
Ruiz, J., Williams, J.P., Dohm, J.M., Fernández, C., López, V., 2009. Ancient heat flows and crustal thickness at Warrego rise, Thaumasia Highlands, Mars: implications for a stratified crust. Icarus 203, 47–57.
Ruiz, J., McGovern, P.J., Jiménez-Díaz, A., López, V., Williams, J.P., Hahn, B.C., Tejero, R., 2011. The thermal evolution of Mars as constrained by paleo-heat flows. Icarus 215, 508–517. https://doi.org/10.1016/j.icarus.2011.07.029.
Ruiz, J., Jiménez-Díaz, A., Egea-González, I., Parro, L.M., Mansilla, F., 2019. Comments on "Using the viscoelastic relaxation of large impact craters to study the thermal history of Mars" (Karimi et al., 2016, Icarus 272, 102-113) and "Studying lower crustal flow beneath Mead basin: implications for the thermal history and rheology of Venus" (Karimi and Dombard, 2017, Icarus 282, 34-39). Icarus 322, 34–39.
Schultz, R.A., 2003. Seismotectonics of the Amenthes Rupes thrust fault population, Mars. Geophys. Res. Lett. 30 (6).
Schultz, R.A., Tanaka, K.L., 1994. Lithospheric-scale buckling and thrust structures on Mars: the Coprates rise and south Tharsis ridge belt. J. Geophys. Res.: Planets 99 (E4), 8371–8385.
Schultz, R.A., Watters, T.R., 2001. Forward mechanical modeling of the Amenthes Rupes thrust fault on Mars. Geophys. Res. Lett. 28 (24), 4659–4662.
Smith, D.E., Zuber, M.T., Frey, H.V., Garvin, J.B., Head, J.W., Muhleman, D.O., et al., 2001. Mars orbiter laser altimeter—experiment summary after the first year of global mapping of Mars. J. Geophys. Res. 106 (E10), 23689–23722.
Tanaka, K.L., Golombek, M.P., Banerdt, W.B., 1991. Reconciliation of stress and structural histories of the Tharsis region of Mars. J. Geophys. Res.: Planets 96 (E1), 15617–15633.
Watters, T.R., 1993. Compressional tectonism on Mars. J. Geophys. Res. 98 (E9) https://doi.org/10.1029/93JE01138, 17,049–17,060.
Watters, T.R., Robinson, M.S., 1999. Lobate scarps and the Martian crustal dichotomy. J. Geophys. Res. 104, 18,981–18,990.
Watters, T.R., Schultz, R.A., Robinson, M.S., 2000. Displacement-length relations of thrust faults associated with lobate scarps on Mercury and Mars: comparison with terrestrial faults. Geophys. Res. Lett. 27 (22), 3659–3662. https://doi.org/10.1029/2000GL011554.
Watters, T.R., Schultz, R.A., Robinson, M.S., Cook, A.C., 2002. The mechanical and thermal structure of Mercury's early lithosphere. Geophys. Res. Lett. 29, 37–31.
Wieczorek, M.A., et al., 2022. InSight constraints on the global character of the Martian crust. J. Geophys. Res.: Planets 127, e2022JE007298. https://doi.org/10.1029/2022JE007298.
Williams, N.R., Watters, T.R., Pritchard, M.E., Banks, M.E., Bell, J.F., 2013. Fault dislocation modeled structure of lobate scarps from Lunar Reconnaissance Orbiter Camera digital terrain models. Journal of Geophysical Research, Planets 118, 224–233.
Ziesch, J., Tanner, D.C., Krawczyk, C.M., 2014. Strain associated with the Fault-Parallel Flow algorithm during kinematic fault displacement. Math. Geosci. 46, 59–73.